

---


# EVENT BLOB TRACKING: AN ASYNCHRONOUS REAL-TIME ALGORITHM

---

PREPRINT\*

 **Ziwei Wang**

Systems Theory and Robotics Group  
Australian National University  
ACT, 2601, Australia  
ziwei.wang1@anu.edu.au

 **Timothy Molloy**

Systems Theory and Robotics Group  
Australian National University  
ACT, 2601, Australia  
timothy.molloy@anu.edu.au

 **Pieter van Goor**

Systems Theory and Robotics Group  
Australian National University  
ACT, 2601, Australia  
pieter.vangoor@anu.edu.au

 **Robert Mahony**

Systems Theory and Robotics Group  
Australian National University  
ACT, 2601, Australia  
robert.mahony@anu.edu.au

July 21, 2023

## ABSTRACT

Event-based cameras have become increasingly popular for tracking fast-moving objects due to their high temporal resolution, low latency, and high dynamic range. In this paper, we propose a novel algorithm for tracking event blobs using raw events *asynchronously* in real time. We introduce the concept of an *event blob* as a spatio-temporal likelihood of event occurrence where the conditional spatial likelihood is blob-like. Many real-world objects generate event blob data, for example, flickering LEDs such as car headlights or any small foreground object moving against a static or slowly varying background. The proposed algorithm uses a nearest neighbour classifier with a dynamic threshold criteria for data association coupled with a Kalman filter to track the event blob state. Our algorithm achieves highly accurate tracking and event blob shape estimation even under challenging lighting conditions and high-speed motions. The microsecond time resolution achieved means that the filter output can be used to derive secondary information such as time-to-contact or range estimation, that will enable applications to real-world problems such as collision avoidance in autonomous driving.

### Project URL:

<https://github.com/ziweiWWANG/Event-Blob-Tracking>

**Keywords** Computer Vision for Automation, Aerial Systems: Perception and Autonomy, Visual Tracking, Event-based Camera, Event blob, Target Tracking, Asynchronous Filtering, Real-time Processing, Time to Contact, Range Estimation, High Dynamic Range.

## 1 Introduction

Object tracking is a core capability for a wide-range of robotics and computer vision applications such as simultaneous localisation and mapping (SLAM), visual odometry (VO), obstacle avoidance, collision avoidance, autonomous driving, virtual reality, smart cities, *etc* [1]. Real-time visual tracking of high-speed targets in complex environments and in low light poses significant challenges due to their fast movement and complex visual backgrounds. In many applications, visual size and shape of the target must be estimated in parallel. Such real-time tracking and estimation is challenging in its own right, but also introduces significant complexity in the preliminary data association problem. Traditional frame-based tracking methods are often hardware-limited as images are susceptible to motion blur, low frame rates and low dynamic range. Event cameras offer significant advantages in these scenarios. Instead of accumulating brightness within a fixed frame rate for all pixels, event cameras capture only changing

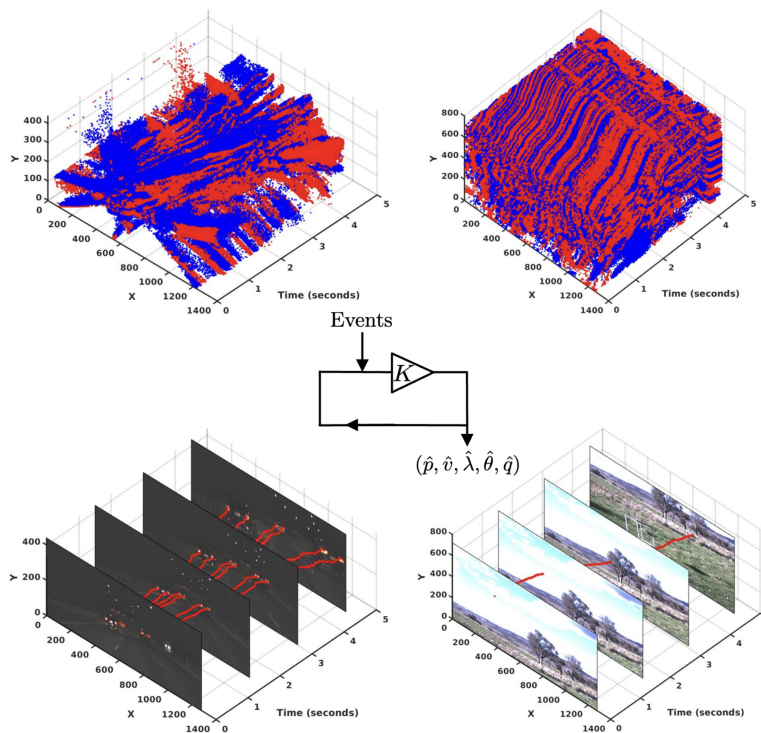


Figure 1: Our event blob tracker leverages asynchronous raw events (top row) to provide high-bandwidth estimates of an event blob’s position ( $p$ ), linear ( $v$ ) and angular ( $q$ ) velocity, orientation ( $\theta$ ), and shape ( $\lambda$ ) information. The filter operates effectively in challenging scenarios including high-speed motions and extreme lighting conditions, and yields state updates up to microsecond resolution depending on event rates. Potential applications include tracking automotive lights (left bottom) or aerial vehicles (right bottom). The high temporal resolution and shape estimation provided by the filter enable downstream data processing such as time-to-contact (TTC) and range estimation.

brightness at a pixel-by-pixel level. Quickly moving foreground objects generate more events than complex visual backgrounds making the event camera sensor modality ideal for high-performance real-world target tracking.

In this paper, we propose an asynchronous real-time target tracking algorithm for event data. The targets considered are modelled as a spatio-temporal event likelihood where the conditional spatial likelihood is blob-like, a structure we term an **event blob** [2]. The event blob concept fundamentally includes the temporal aspect of event data. In particular, if a temporal window of event data is accumulated, the resulting pseudo image will be a blurred version of the spatial likelihood of the event blob due to the temporal motion of the blob. The approach taken is to use a spatial Gaussian likelihood with time-varying mean and covariance to model the unipolar event blob (where both polarities are equally considered). The state considered includes position (mean of the event blob), non-homogeneous spatial cross-correlation of the event blob (encoded as two principle correlations and an orientation), and both the linear and angular velocity of the blob. The algorithm uses an extended Kalman filter that accepts raw event data and uses each event directly to update a stochastic state-estimate asynchronously. A key novelty of the algorithm is that the filter states for the shape of the distribution are used as stochastic parameters in the generative measurement model. This formulation is non-standard in classical extended Kalman filters. To do this we construct two pseudo measurement functions based on normalised position error and chi-squared variance. These pseudo measurements provide information on the spatial variance of the event blob and ensure observability of the shape parameters of the target. The asynchronous filter state is updated for every event received (associated with a given blob), coupling the filter update rate to the raw event rate of the blob tracked. For scenarios with low background noise, the foreground event rate is limited only by the microsecond physical limits of the camera (data bus, circuit noise and refractory period limitations of the camera *etc* [3]) and, even in poor light conditions, filter updates in excess of 50kHz are possible.

We evaluate the proposed algorithm on two real-world case studies, tracking automotive tail lights at night, and tracking a quickly moving aerial vehicle. In the first case study, we track multiple automotive tail lights in a night driving scenario. Due to the high event rates induced by the flickering LED lights, the filter achieves update rates of over 100kHz with high signal-to-noise ratio. The quality of the filter data is validated by computing robust, high-bandwidth, time-to-contact estimates from the visual divergence between tail lights on a target vehicle. In the second case study, we track and estimate the event distribution of a high-speed aerobatic rotor in difficult visual conditions and in front of complex visual backgrounds. The visual shape estimation of the target event blob is used to infer range information demonstrating the utility of the shape parameter estimation and quality of the filter estimate.

The primary contributions of the paper are:

- A novel asynchronous Kalman filter for real-time high-frequency event blob tracking.
- A novel modification of extended Kalman filter theory to estimate shape parameters of event blob targets.
- Demonstration of the performance of the proposed algorithm on two real-world case studies with challenging datasets. The datasets are provided open-source for future comparisons.

## 2 Related Works

Event cameras have been used in a range of blob-like object tracking applications including; star tracking [4, 5, 6], high-speed particle tracking [7, 8, 9] and real-time eye tracking [10, 11]. The tracking algorithms developed for these applications have, in the most part, been bespoke with a limited ability to generalise to other scenarios. General-purpose event-based tracking algorithms have focused on corner and template tracking. The corner tracking algorithms can be categorised into window-based data association or clustering methods [12, 13, 14, 15, 16], asynchronous event-only methods [17, 18, 19, 20, 21, 22], and asynchronous methods that use hybrid event-frame data [23, 22]. Template-based methods for event cameras tend to be highly dependent on the scenario. Mueggler *et al.* [24] used a stereo event camera to detect and track spherical objects for collision avoidance. Mitrokhin *et al.* [25] estimated relative camera motion from a spatio-temporal event surface, then segmented and tracked moving objects based on the mismatch of the local event surface. Falanga *et al.* [26, 27] demonstrated the importance of low latency for sense-and-avoid scenarios. Their experiments used 10ms windowed event data and classical blob tracking algorithms. Sanket *et al.* [28] developed an onboard neural network for the same sense-and-avoid scenario. Rodriguez-Gomez *et al.* [29] used asynchronous corner tracking and then clustered corners to create objects that are tracked. Li *et al.* [30] and Chen *et al.* [31] converted event streams into pseudo-frames and then tracked objects using frames. Recent work has seen considerable effort in deep learning methods for object tracking [32, 33, 28, 34, 35]. The combination of conventional frames and event cameras has also been explored for object tracking [36, 37], enabling the use of data association techniques derived from classical computer vision literature. Active LED lights are commonly used to create event blob targets for experimental work. Müller *et al.* [38] used LED markers in a low-power embedded DVS system and introduced two active LED marker tracking algorithms based on event counting and the time interval between events. Censi *et al.* [39] mounted LED markers on a flying robot and proposed a low-latency tracking method that associated LED markers based on the time interval between events and then tracked each LED light using a particle filter. Wang *et al.* [40] used active LED lights for high-speed visual communication with conventional blob detection and tracking method on pseudo-frames. These LED tracking methods usually require the targets to blink in known or very high frequencies. A characteristic of the schemes discussed is that data association is mostly built into an asynchronous pre-processing module, such as a corner detector, clustering algorithm or frame-based correlation; or the algorithm requires pseudo-frames, event-frames or estimation of an event surface over a window of data. Such architectures lead to increased latency and reduced frequency response of target tracking, although many of the algorithms reviewed still achieve excellent results, especially when compared to classical frame-based image tracking.

## 3 Problem Formulation

In this section we formulate the problem of tracking event blob targets.

### 3.1 Spatio-Temporal Gaussian Likelihood Model for Event Blob Targets

Event cameras report the relative log intensity change of brightness for each pixel asynchronously. We consider the likelihood  $\ell(\xi, t, \rho)$  of an event occurring at pixel location  $\xi \in \mathbb{R}^2$  at time  $t \geq 0$  and with polarity  $\rho \in \{\pm 1\}$ . We will term such a likelihood model an event blob if the spatial distribution of the conditional likelihood  $\ell(\xi, \rho|t)$  for a fixed time  $t$  is blob-like. A spatio-temporal Gaussian event blob likelihood function is given by

$$\begin{aligned} \ell(\xi, t, \rho) \\ := \frac{\gamma(t)B(\rho)}{2\pi\sqrt{\det(\Lambda(t))}} \exp\left(-\frac{1}{2}(\xi - p(t))^\top \Lambda(t)^{-1}(\xi - p(t))\right), \end{aligned} \quad (1)$$

where  $p(t) \in \mathbb{R}^2$  is the pixel location of the centre of the object and  $\Lambda(t) \in \mathbb{R}^{2 \times 2}$  is the shape of the object (encoded as the second-order moment of the event spatio-temporal intensity). The positive-definite matrix  $\Lambda(t) > 0$  is written

$$\Lambda(t) := R(\theta(t)) \begin{pmatrix} \lambda^1(t) & 0 \\ 0 & \lambda^2(t) \end{pmatrix} R^\top(\theta(t)) \quad (2)$$

for principle correlations  $\lambda^1(t), \lambda^2(t) > 0$  and orientation angle  $\theta(t)$  where  $R(\theta(t))$  is the associated rotation matrix. The scalar  $\gamma(t)$  encodes the temporal dependence of the likelihood associated with changing event rate and  $B(\rho)$  denotes a binomial distribution associated with whether the event has polarity  $\{\pm 1\}$ . If  $\gamma$  is integrable on a time interval of interest, then the spatio-temporal Gaussian event blob likelihood could be normalised to produce a probability density on this time interval. In this

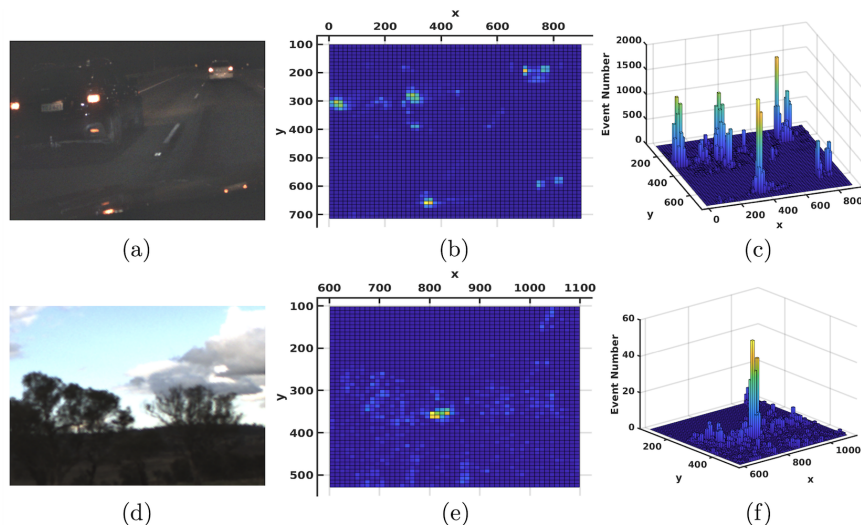


Figure 2: An example of plotting a short temporal window of events in a histogram pseudo-frame for the two case studies considered in the paper. In the upper row, the LED car tail lights create a collection of event blobs. (Note the reflections of the lights in the bonnet of the experimental car.) In the bottom row, a quadrotor is flying in front of the trees and is difficult to pick out of the RGB image but generates an event blob that is clearly visible in (e) and (f). The leading and trailing edges of the event blob can be seen in (e), while the overall blob structure is visible in (f).

paper, however, we will use the conditional likelihood  $\ell(\xi, \rho|t_k)$  for  $t = t_k$ , a spatial Gaussian distribution with time-varying parameters. In the sequel, we will often omit the time index from the state variables  $p = p(t)$ ,  $\theta = \theta(t)$ , *etc.*, to make the notation more concise.

The archetypal examples of event blob targets are flickering objects such as an LED or fluorescent light [41], a spinning rotor or wheel, a fluttering flag or cloth, *etc.* A flickering target generates events at pixel locations in proportion to the frequency of the flicker and intensity of the source at that pixel. The likelihood of an event occurring at a given moment in time is proportional to the rate of events. Thus, for a target with constant flicker, the spatial distribution of the associated event blob likelihood is directly related to the intensity of the source and is analogous to image intensity. An example of the event arrival histogram for LED tail lights of cars is shown in the top row of Figure 2. Here the image blobs in the histogram Figure 2b are roughly Gaussian.

In the case of a non-flickering target, the situation is more complex since the motion of the target in the image plane is required to generate events. In this case, the events are asymmetrically arranged around the target centre depending on whether the target is bright or dark with respect to the background. For a bright target against a dark background, the events in the direction of motion are positive while the trailing events are negative, and vice-versa if the background is brighter than the target. If both positive and negative events are equally considered, then the resulting density is symmetric around the centre point of the target (for an idealised sensor). The rate of events at the target centre should be zero since the intensity of the target blob at this point is a maximum (or minimum) with respect to the direction of motion of the target. For most targets the image gradient remains high until close to the centre of the target and separating the leading and trailing event clusters is difficult [42, 6]. The second row of Figure 2 provides a good example of a non-flickering moving target. The density of events in Figure 2f clearly shows the leading and trailing edge effects where the target is moving to the left and down in the image. The effective likelihood over the whole target, however, appears to be a single blob as seen in Figure 2e.

In practice, we have found that a simple event blob model and the associated spatio-temporal Gaussian likelihood model proposed in (1) works well for a wide range of blob-like intensity targets.

### 3.2 Event Generation Model

Consider a sequence of events  $e_k := (\xi_k, t_k, \rho_k)$  at pixel locations  $\{\xi_k\}$ , times  $\{t_k\}$  and with polarities  $\{\rho_k\}$  associated with a target event blob modelled by (1). We will consider the unipolar model for event blobs where the polarity  $\rho_k$  is ignored and all events are considered equally. The associated likelihood is the marginal

$$\ell(\xi_k, t_k) = \sum_{\rho_k \in \{\pm 1\}} \ell(\xi_k, t_k, \rho_k).$$

In addition, we will ignore noise in the time-stamp and consider the conditional likelihood  $\ell(\xi|t = t_k)$  fixing time at  $t = t_k$ . With modern event cameras, where the time resolution is as low as  $1\mu\text{s}$  resolution this assumption is justified in a wide range of scenarios. Based on these assumptions then a generative noise model for the event location is given by

$$\xi_k = p(t_k) + \Lambda(t_k)\eta_k, \quad \eta_k \sim \mathcal{N}(0, I_2), \quad (3)$$

where coordinate  $p(t_k)$  is the true location of the object and we emphasise that the times  $\{t_1, t_2, \dots, t_k, \dots\}$  are not periodic and depend on the asynchronous time-stamp of each event. The measurement noise  $\eta_k$  is a zero-mean independent identically distributed (i.i.d.) Gaussian process with known covariance. The noise process is scaled through the covariance  $\Lambda(t_k)$  given by (2) with parameters  $\lambda^1(t_k), \lambda^2(t_k) > 0$  and  $\theta(t_k)$ .

### 3.3 System Model

The proposed model considers the states  $p = (p_x, p_y)$  for the object centre, and the shape parameters  $(\lambda^1, \lambda^2)$  and  $\theta$ . The parameter  $\theta$  can be thought of as a spatial state parameter describing the orientation of the object, while the principle correlations  $\lambda = (\lambda^1, \lambda^2)$  encode the eigenvalues of the second-order ‘visual’ moment of the object. We add a linear velocity state  $(v^x, v^y)$  and angular velocity  $q$  for the spatial states  $(p_x, p_y, \theta)$ . We model uncertainty in the state evolution using continuous random walk Wiener processes. The proposed state model is

$$dp = v(t)dt + dw_p, \quad w_p \sim \mathbf{W}(Q^p), \quad (4a)$$

$$dv = dw_v, \quad w_v \sim \mathbf{W}(Q^v), \quad (4b)$$

$$d\theta = q(t)dt + dw_\theta, \quad w_\theta \sim \mathbf{W}(Q^\theta), \quad (4c)$$

$$dq = dw_q, \quad w_q \sim \mathbf{W}(Q^q), \quad (4d)$$

$$d\lambda = dw_\lambda, \quad w_\lambda \sim \mathbf{W}(Q^\lambda). \quad (4e)$$

Here  $Q^p, Q^v, Q^\lambda \in \mathbb{R}^2$  and  $Q^\theta, Q^q \in \mathbb{R}^1$  are positive definite matrices and  $\mathbf{W}(Q)$  denotes a Wiener process with variance  $Q$ . The state vector  $x$  is

$$x := (p, v, \theta, q, \lambda) \in \mathbb{R}^8. \quad (5)$$

## 4 Asynchronous Object Dynamics and Proposed Pseudo Measurement Construction

### 4.1 Asynchronous Object Dynamics

Let  $\{e_k\}$  be a sequence of events and define the asynchronous-time state

$$\begin{aligned} x_k := x(t_k) &= (p(t_k), v(t_k), \theta(t_k), q(t_k), \lambda(t_k)) \\ &=: (p_k, v_k, \theta_k, q_k, \lambda_k) \end{aligned}$$

for each timestamp  $t_k$  drawn from the events. Integrating (4) one obtains

$$x_k = F_k x_{k-1} + w_k, \quad w_k \sim \mathcal{N}(0, Q_k), \quad (6)$$

where  $w_k$  is Gaussian noise with

$$Q_k = \delta_t^k \text{diag}(Q^p \quad Q^v \quad Q^\lambda \quad Q^\theta \quad Q^q), \quad (7)$$

where

$$\delta_t^k = t_k - t_{k-1} \quad (8)$$

is the time interval. The state transition matrix is

$$F_k = \begin{pmatrix} 1 & 0 & \delta_t^k & 0 & 0 & 0 & 0 & 0 \\ 0 & 1 & 0 & \delta_t^k & 0 & 0 & 0 & 0 \\ 0 & 0 & 1 & 0 & 0 & 0 & 0 & 0 \\ 0 & 0 & 0 & 1 & 0 & 0 & 0 & 0 \\ 0 & 0 & 0 & 0 & 1 & 0 & 0 & 0 \\ 0 & 0 & 0 & 0 & 0 & 1 & 0 & 0 \\ 0 & 0 & 0 & 0 & 0 & 0 & 1 & \delta_t^k \\ 0 & 0 & 0 & 0 & 0 & 0 & 0 & 1 \end{pmatrix}. \quad (9)$$

Note that since the continuous-time process had a Wiener noise process, the additive noise  $w_k$  is a Gaussian distribution with covariance that grows linearly with event time interval  $\delta_t^k$  [43].

### 4.2 Two-Stage Pseudo Measurement Construction

The natural measurement available for event blob target tracking is the location  $\xi_k$  of each event  $e_k = (\xi_k, t_k, \rho_k)$ . The associated generative noise model for the raw event location measurement is given by (3). However, this model cannot be used directly in the proposed event-blob target tracking filter since the uncertainty  $\Lambda_k$  in the generative noise model is itself a state of the filter (i.e., determined by variables  $\lambda_k, \theta_k$  in  $x_k$ ). Instead, we will derive a pseudo measurement with known measurement covariance and use the theory of Kalman filtering with constraints [44].

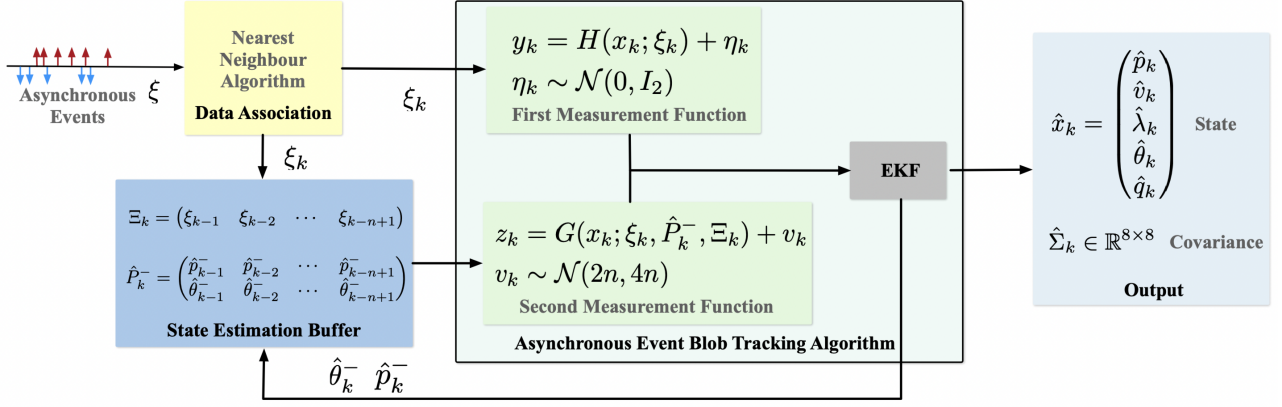


Figure 3: Block diagram of our asynchronous event blob tracking algorithm.

Define a measurement function by

$$H(x_k; \xi_k) := \Lambda_k^{-1}(\xi_k - p_k), \quad (10)$$

where  $H$  is a function of the state  $x_k$  parametrised by the measurement  $\xi_k$ . Recalling (3) then by construction

$$H(x_k; \xi_k) = \Lambda_k^{-1}(\xi_k - p_k) = \eta_k,$$

where  $\eta_k \sim \mathcal{N}(0, I_2)$  is an independent identically distributed (i.i.d.) Gaussian process with known covariance. In particular, the expected value  $E[\Lambda_k^{-1}(\xi_k - p_k)] = 0$ .

Define a new measurement model

$$y_k = H(x_k; \xi_k) + \eta_k, \quad \eta_k \sim \mathcal{N}(0, I_2) \quad (11)$$

with pseudo measurements  $y_k \equiv 0 \in \mathbb{R}^2$ . The generative noise model (11) with measurements  $y_k = 0$  has known stochastic parameters  $\eta_k \sim \mathcal{N}(0, I_2)$  and can be used in a Kalman filter construction.

The new measurement function  $H(x_k; \xi_k)$  (10) is non-linear in the state  $x_k$  while the original measurement relationship (3) was linear. Consequently, it is necessary to use an extended Kalman filter implementation where the output model (10) is linearised around the present estimate of the state.

The measurement (11) is insufficient to provide observability of the full state  $x_k$ . Intuitively, this can be seen by noting that a decreasing measurement error  $\|y_k - \Lambda_k^{-1}(\xi_k - p_k)\| = \|\Lambda_k^{-1}(\xi_k - p_k)\|$  can be modelled either as indicating  $p_k$  should be moved towards  $\xi_k$  or that  $\Lambda_k$  should be increased. To ensure full system observability, we introduce an additional pseudo measurement specifically designed to observe the shape parameter  $\Lambda_k$ . The approach is to construct a chi-squared statistic from a buffer of prior state estimates that allows estimation of the shape parameters  $\lambda_k = (\lambda_k^1, \lambda_k^2)$ .

Assume that the extended Kalman filter has been operating on  $n$  samples, with  $n$  events received for the target, and a bootstrap filter run on the initial  $n$  timestamps  $t_k$  to enable a warm start for the full filter. For a fixed index  $k$  and window length  $n$ , let  $\hat{p}_{k-j+1}^-$  and  $\hat{\theta}_{k-j+1}^-$  denote the state-estimate filter predications based on measurements  $\xi_{k-j+1}$ , where  $j = (2, \dots, n)$ . The minus sign indicates that the filter estimate is taken after the predict step but before the update step. Define  $\hat{P}_k^-$  to be the buffer of state prediction estimates

$$\hat{P}_k^- := \begin{pmatrix} \hat{p}_{k-1}^- & \hat{p}_{k-2}^- & \cdots & \hat{p}_{k-n+1}^- \\ \hat{\theta}_{k-1}^- & \hat{\theta}_{k-2}^- & \cdots & \hat{\theta}_{k-n+1}^- \end{pmatrix}, \quad (12)$$

and  $\Xi_k$  to be the buffer of the associated events

$$\Xi_k := (\xi_{k-1} \quad \xi_{k-2} \quad \cdots \quad \xi_{k-n+1}). \quad (13)$$

For  $j = (2, \dots, n)$ , define

$$\hat{\Lambda}_{k-j+1} := \mathcal{R}(\hat{\theta}_{k-j+1}^-) \text{diag}[\lambda_k^1, \lambda_k^2] \mathcal{R}(-\hat{\theta}_{k-j+1}^-), \quad (14)$$

where  $(\lambda_k^1, \lambda_k^2)$  are the principle correlations at time  $k$ , while the prior filter states are used to rotate the image moment to the best estimate of its orientation. Note that we do not use all the available data at time  $k$  for the estimation of  $\hat{\theta}_{k-j+1}^-$  since doing so would introduce undesirable stochastic dependencies (cf. proof of Lemma 4.1).

Let  $\beta \geq \|\Sigma_{\hat{p}_{k-j+1}}^-\|_2$  be a constant estimate of an over-bound for the uncertainty in  $\hat{p}_{k-j+1}$ . Define

$$\chi_{k-j+1} := \frac{1}{1+\beta} \hat{\Lambda}_{k-j+1}^{-1} (\xi_{k-j+1} - \hat{p}_{k-j+1}). \quad (15)$$

Note that  $E[\hat{p}_{k-j+1}^-] = p_{k-j+1}$  and  $E[\hat{\Lambda}_{k-j+1}^-] = \Lambda_{k-j+1}$ . Replacing the estimates in (16) by their expected values yields a scaled version of the event generation model (3). Thus, the primary contribution to the uncertainty in  $\chi$  will be a Gaussian distribution  $\mathcal{N}(0, \frac{1}{1+\beta} I_2)$ . Variance in  $\hat{p}_{k-j+1}^-$  is bounded by the estimated parameter  $\beta > 0$ . Since this variance has a similar structure to the variance in  $\xi_k$  it can be approximated as contributing additional uncertainty  $\frac{\beta}{1+\beta} I_2$  to  $\chi_{k-j+1}$ . The additional uncertainty in  $\hat{\theta}_{k-j+1}^-$  is only present in the rotation matrix  $\mathcal{R}(\hat{\theta}_{k-j+1}^-)$  and its contribution to uncertainty in  $\chi$  is negligible. Thus, the uncertainty in  $\chi$  can be modelled by

$$\chi_{k-j+1} \sim \mathcal{N}(0, \frac{1}{1+\beta} I_2 + \frac{\beta}{1+\beta} I_2) = \mathcal{N}(0, I_2).$$

Define a new virtual output function  $G$

$$G(x_k; \xi_k, \hat{P}_k^-, \Xi_k) := \|\Lambda_k^{-1} (\xi_k - p_k)\|^2 + \sum_{j=2}^n \|\chi_{k-j+1}\|^2. \quad (16)$$

Since  $\chi_{k-j+1}$  and  $\Lambda_k^{-1} (\xi_k - p_k)$  are normally distributed with unit covariance, the output function  $G(x_k; \xi_k, \hat{P}_k^-, \Xi_k)$  is the sum of the squares of  $n$  independent 2-dimensional Gaussian random variables. Consequently, it follows a chi-squared distribution with an order of  $2n$ . According to the central limit theorem [45], as  $n$  becomes sufficiently large, the chi-squared distribution converges to a normal distribution with a mean of  $2n$  and a variance of  $4n$ . Based on this, we propose a pseudo measurement model

$$z_k := G(x_k; \xi_k, \hat{P}_k^-, \Xi_k) + v_k, \quad v_k \sim \mathcal{N}(2n, 4n), \quad (17)$$

with pseudo measurements  $z_k \equiv 2n$ .

This development depends on the bound  $\beta \geq \|\Sigma_{\hat{p}_{k-j+1}}^-\|_2$ . In practice, the uncertainty in  $\hat{p}_{k-j+1}$  is often much smaller compared to the uncertainty in the event position  $\xi_k$  associated with the actual shape of the object. Typically  $\Lambda_k$  is 100 to 1000 larger than  $\Sigma_{\hat{p}_k}^-$ , corresponding to a  $\beta \in [10^{-2}, 10^{-3}]$ . Although this bound makes little difference in practice, it provides theoretical certainty that the filter will not become overconfident.

The two pseudo measurements  $y_k$  (11) and  $z_k$  (17) provide sufficient information for the observability of the system. However, as these measurements are reconstructed from state and filter information, it is necessary to characterise any stochastic dependencies between them. In appendix Section 9.1, we provide a proof of the independence of  $H_k$  and  $G_k$  which demonstrates that the covariance of the off-diagonal terms in the joint measurement covariance to be zero.

**Lemma 4.1.** *The virtual measurement*

$$m_k = \begin{pmatrix} y_k \\ z_k \end{pmatrix} = \begin{pmatrix} 0 \\ 0 \\ 2n \end{pmatrix} \in \mathbb{R}^3 \quad (18)$$

has the generative noise model

$$m_k = \begin{pmatrix} H(x_k; \xi_k) \\ G(x_k; \xi_k, \hat{P}_k^-, \Xi_k) \end{pmatrix} + \nu, \quad \nu \sim \mathcal{N}(0, R) \quad (19)$$

$$R = \begin{pmatrix} I_2 & 0 \\ 0 & 4n \end{pmatrix}. \quad (20)$$

## 5 Asynchronous Tracking Filter

In this section, we exploit our construction of the object dynamics and pseudo measurements from the previous section to construct an efficient (asynchronous) tracking filter, along with its track-initialisation and data association logic.

### 5.1 Extended Kalman Filter for Tracking

We linearise the two non-linear measurement models  $y_k$  and  $z_k$  (11)-(17) by computing the Jacobian matrix of the  $H(x_k; \xi_k)$  and  $G(x_k; \xi_k, \hat{P}_k^-, \Xi_k)$  measurement function. The linearised observation model  $C_k$  for the state  $x_k$  is written

$$C_k = \begin{pmatrix} C_k^H \\ C_k^G \end{pmatrix} \in \mathbb{R}^{3 \times 8}. \quad (21)$$

The detailed partial derivatives are shown in Appendix 9.2.

From here we follow the standard extended Kalman filter algorithm to compute the pre-fit residual Kalman filter gain  $K_k$  as

$$K_k = \hat{\Sigma}_k^- C_k (C_k \hat{\Sigma}_k^- C_k^\top + R)^{-1}. \quad (22)$$

Finally, the updated state estimate and covariance estimate are given by

$$\hat{x}_k = \hat{x}_k^- + K_k \tilde{y}_k, \quad (23)$$

$$\hat{\Sigma}_k = (I - K_k C_k) \hat{\Sigma}_k^-. \quad (24)$$

Note that although the underlying process is asynchronous, the update has been expressed as a discrete time system model with time-varying state matrix and the standard extended Kalman filter discrete time algorithm can be applied.

## 5.2 Track Initialisation

The second pseudo measurement function (16) requires  $n - 1$  historic filter states and cannot be used initially. We initialise the filter with just the measurement  $y_k$  for the first  $n - 1$  events and then switch to the full filter once the state buffer is full. The estimate of  $(\hat{\lambda}^1, \hat{\lambda}^2)$  is not observable during this period. However, due to the short transient period ( $< 1$  ms) and slow drift in these state estimates, the start up procedure has a negligible effect on the overall filter response.

## 5.3 Data Association

Data association in visual target tracking is arguably one of the most difficult problems. In this paper, we take a simple approach that considers all events in a neighbourhood of the event blob to be inliers. As long as the signal-to-noise ratio of the number of events generated by an event blob target to the background noise events is high enough, the disturbance from background noise events will be small and the filter will maintain track. Furthermore, any background noise events that are spatially homogeneous, such as an overall change of illumination, will be distributed in the developed pseudo measurements and will have only a marginal effect on the filter tracking performance. It is only when two objects generating a large number of events cross in the image that the algorithm may lose track. This may be due to two flickering targets crossing in the image, such as when the tail lights from one car occlude the tail lights of another car. Or when the ego-motion of the camera causes a high-contrast background feature to cross behind a low-intensity target. It may be possible to address the second case by ego-motion estimation for the camera, however, that is beyond the scope of the present paper.

There remains the question of choosing the neighbourhood in which to associate inliers and outliers. The size of this neighbourhood must be adapted dynamically to adjust for the changing size of the flickering target in the image. Our data association approach uses the nearest neighbour classifier with a dynamic threshold  $\sigma$ . That is, any event  $\xi_k$  that lies less than  $\sigma$  pixels from the predicted state estimate  $\hat{p}_k^-$  is associated with the target and used in the filter. The threshold  $\sigma$  is chosen as a low-pass version of  $\max(\hat{\lambda}_k^1, \hat{\lambda}_k^2)$ . In continuous-time, this low-pass filter is written

$$\dot{\sigma}(t) = -\alpha\sigma(t) + b\alpha \max(\hat{\lambda}_k^1, \hat{\lambda}_k^2), \quad (25)$$

where  $\alpha$  is the filter gain and  $b$  is the desired ratio between the distance threshold and the estimated target size. Integrating (25) over the time interval  $\delta t_k = t_k - t_{k-1}$  for  $\max(\hat{\lambda}_k^1, \hat{\lambda}_k^2)$  constant yields

$$\begin{aligned} \sigma_k &= \beta_k \sigma_{k-1} + b(1 - \beta_k) \max(\hat{\lambda}_k^1, \hat{\lambda}_k^2), \\ \beta_k &:= \exp(-\alpha(t_k - t_{k-1})). \end{aligned} \quad (26)$$

The gain  $\alpha$  is chosen based on the expected continuous-time dynamics of the target in the image.

## 5.4 Computational Cost

Our tracking method includes two main steps: data association and the extended Kalman filter. The data association step has a linear event complexity of  $O(N)$  for  $N$  input events, effectively passing only a subset of  $M$  events to the extended Kalman filter, where  $M \ll N$ . The extended Kalman filter operates with a time complexity of  $O(nM)$ , where  $n$  denotes the buffer length in (12)-(13). In practice, the buffer length is typically set to  $n < 20$ , and it is worth noting that  $N$  remains significantly larger than  $nM$ . As a result, our algorithm maintains an overall linear event complexity of  $O(N)$ .

Since the data association step only scales linearly with the event rate and this process significantly reduces the number of events used in the Kalman filter, the algorithm is highly efficient for real-time implementation. The efficiency and asynchronous processing of the method make it well-suited for implementation on pixel-by-pixel front-end hardware, such as FPGA and ASIC. Such systems have the potential to be particularly advantageous for high-performance embedded robotic systems.



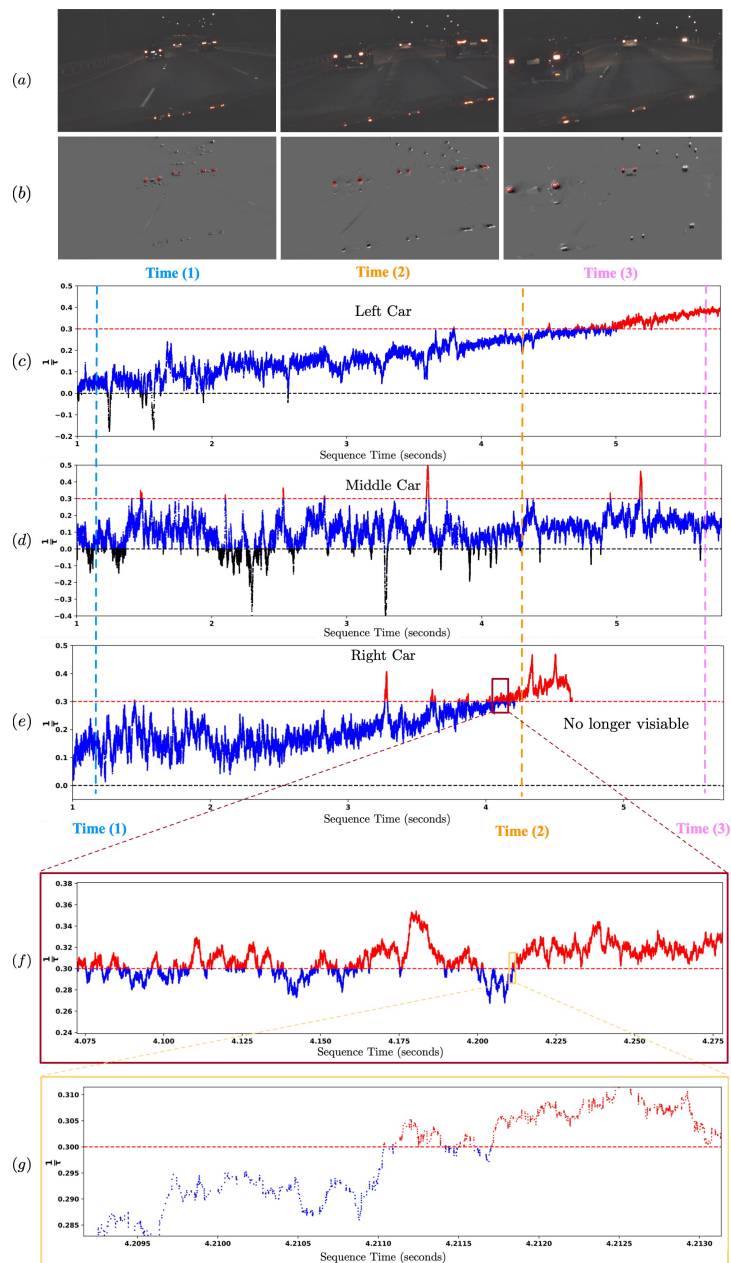


Figure 4: Multi-vehicle tail lights tracking and time-to-contact (TTC) experiments. Three cars are visible beneath street lights on a multi-lane road. The cars tail lights are reflected in the bonnet of the experimental vehicle. (a). Reference RGB frames. (b). Event reconstructions obtained using the event-based high-pass filter [46]. Tracked objects are marked with red ellipses. (c)-(e). Estimated (inverse) time-to-contact from the three front cars. Blue represents that two cars approaching and black means they are diverging. Red represents that two cars are approaching faster than the safety threshold. The timestamps of the three reference images are marked in three dotted lines. (f) is the zoomed-in view of the red box section in (e), and (g) is the further zoomed-in view of the yellow box section in (f), demonstrating the proposed filter achieves more than 100kHz visual TTC estimation. See more details in the supplementary video.

## 6 Experiments

### 6.1 Dataset Collection Setup

We recorded events and reference frames using a Prophesee Gen4 event camera ( $720 \times 1280$  pixels) and a FLIR RGB camera (Chameleon3USB3,  $2048 \times 1536$  pixels). The two cameras were placed side-by-side and time-synchronised by an external trigger (see Figure 6). The RGB camera frames were re-projected to the event camera image plane using stereo camera calibration.

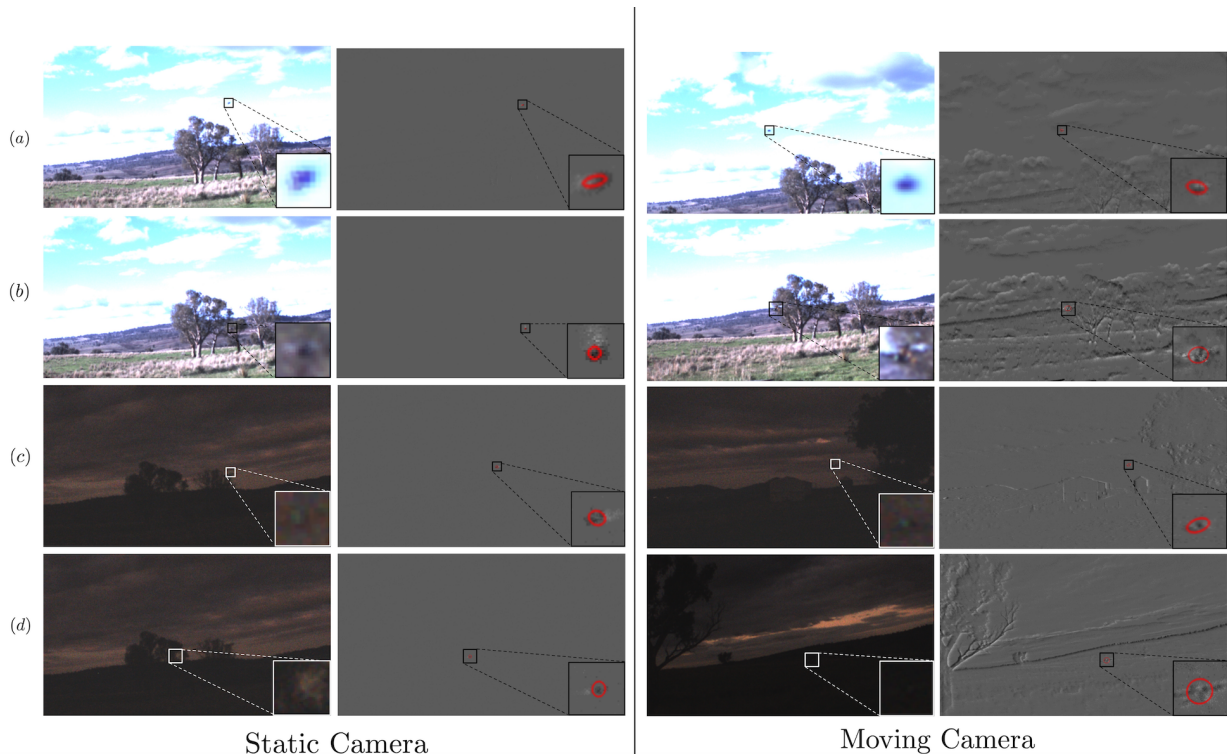


Figure 5: Example of tracking a quadrotor in different lighting conditions and camera motions using only events. Grayscale images are displayed only for reference. The estimated position, size and orientation of the drone are illustrated by red ellipses. Refer to the supplementary video for the tracking performance.



Figure 6: Left: outdoor flying quadrotor experiments. Right: Our quadrotor with an RTK-GPS and our stereo event-frame camera.

Two real-world datasets were collected for evaluation: night driving and outdoor flying quadrotor data. Both datasets include high-speed targets and challenging lighting conditions, allowing a comprehensive evaluation of tracking and shape estimation, as well as for downstream tasks such as time-to-contact estimation and range estimation. For the flying quadrotor dataset, we used a small quadrotor equipped with a real-time kinematic (RTK) positioning GPS (see Figure 6).

## 6.2 Night Driving Data

In this experiment, the event camera system was mounted on a tripod (held down by hand in the foot well) inside a car driving on a public road at night. The proposed algorithm is used to track the tail lights of other vehicles, and we demonstrate its performance by using the output states to estimate time-to-contact (TTC) at more than 100kHz.

### 6.2.1 Time-To-Contact

Time-to-contact (TTC) defines the estimated time before a collision occurs between two objects, typically a vehicle and an obstacle or another vehicle. We estimate inverse TTC, or visual divergence, by tracking both the left and right tail lights of the front cars using the proposed filter. The filter provides high-rate estimates of the position and velocity of the event blobs

associated with the left and right tail lights on each car at time  $t_k$ , denoted as  $\hat{p}_k^L$ ,  $\hat{p}_k^R$ ,  $\hat{v}_k^L$ , and  $\hat{v}_k^R$ , respectively. The visual divergence between the blobs is the ratio of the relative visual velocity between the blobs to visual distance between the blobs in the image. Thus  $1/\tau(t_k)$ , the inverse TTC, can be computed by

$$\frac{1}{\tau(t_k)} := \frac{(\hat{v}_k^L - \hat{v}_k^R)^\top (\hat{p}_k^L - \hat{p}_k^R)}{\|\hat{p}_k^L - \hat{p}_k^R\|^2}. \quad (27)$$

## 6.2.2 Experiments

In Figure 4, we present an example of tracking the tail lights of three cars at night, travelling with an average speed of approximately 90 km/h. The figure displays the reference images captured by an RGB frame-based camera in (a) and the event reconstructions (obtained using the event high-pass filter [46]) in (b) across three different timestamps. Tracked objects are marked with red ellipses. By choosing the bias of the Prophesee Gen4 camera carefully, we are able to preserve events associated with the high-frequency LED lights and reduce background ego-motion events leading to high signal-to-noise event data. This trivialises the data association and enables robust, accurate, high-band width performance of our event blob tracker. Conversely, the RGB reference frames are mostly dark and blurry and obtaining dynamic information on relative motion in the image from this data would be difficult.

We estimate  $\frac{1}{\tau}$ , the inverse time-to-contact (TTC), of the left, middle, and right car and plot them in Figure 4c-e). The timestamps corresponding to the RGB and event images in the top rows are marked in the plots below; timestamps (1), (2), and (3) are distinguished by a blue, orange, and pink dashed line, respectively. A positive  $\frac{1}{\tau}$  indicates that the distance to a given car is decreasing, while a negative  $\frac{1}{\tau}$  indicates that the distance to a given car is increasing (and consequently no collision can occur). For illustrative purposes, we have chosen to indicate a safety threshold at  $\frac{1}{\tau} = 0.3$  when the following car is around 3.3 seconds from collision with the leading car if the velocities were to be kept constant. Values exceeding this are shown in red in Figure 4c-g).

Figure 4d) indicates the experimental vehicle maintaining a relatively constant TTC to the middle car in the same lane, consistent with safe driving margins. Figure 4e) shows the inverse TTC  $\frac{1}{\tau}$  of the right car exceeds the safety threshold at approximately 4.3 seconds, shortly before we overtake it at 4.6 seconds. No TTC data is shown in Figure 4e) after 4.6 seconds since the car is not visible. Then, in Figure 4c), the inverse TTC of the left car exceeds the safety threshold around 5 seconds. See the RGB frames and event reconstructions in Figure 4a)-b) for reference.

Irregularities in the road surface induce bouncing and swaying motion of the vehicle frame that, since the camera is held firmly to the dashboard of the car, lead to horizontal linear velocity of the camera and results in rapid changes in TTC. There are several clear short peaks in 4d), both positive and negative, due to small bumps and depressions in the road surface. For example, the brief 50-millisecond black (negative) peak that appears around 3.3 seconds in Figure 4d) along with the red peak in Figure 4e) would indicate that the left front wheel has encountered a bump inducing the vehicle to pitch backward and sway to the right. The motion can be appreciated in the supplementary video for the full sequence, although since the entire bump sequence occurs in a period of around 50ms the actual motion of the car is correspondingly small.

Figure 4f) provides a zoomed-in view of the red box section in Figure 4e) of 200 milliseconds in length, and Figure 4g) provides a further zoomed-in view of the yellow box section within subplot (f) of 4 milliseconds in length. These plots demonstrate the exceptionally high temporal resolution of our filter, processing updates at more than 100kHz. This remarkable speed minimises latency for vital decision-making processes such as braking and acceleration, particularly in emergency situations. It clearly surpasses the capabilities of frame-based TTC algorithms, which are limited by the frequency of incoming RGB frames (typically around 40Hz), or even pseudo-frame event based algorithms (requiring around 1K to 10K events per pseudo-frame) that would operate in the order of 10-100Hz. This performance, for a single event camera at night and without any additional active sensors like Lidar or Radar, demonstrates the potential of applying event cameras, and the proposed tracking algorithm, to problems in autonomous driving.

## 6.3 Flying Quadrotor Data

We demonstrate the performance of the proposed filter by tracking a flying quadrotor under various camera motions and lighting conditions shown in Figure 5. Figure 5a)-b) demonstrate the tracking performance in well-lit conditions, while data shown in Figure 5c)-d) demonstrate the performance in poorly lit conditions. The RGB images and event reconstruction images are provided for reference only and the filter is implemented on pure asynchronous event data. The red ellipses superimposed on the event reconstruction images illustrate the position, size, and orientation of the quadrotor as estimated by our filter. Please also refer to the supplementary video to see the tracking performance.

The first two columns in Figure 5 show the reference frames and event reconstruction recorded with a stationary camera. In these conditions, the majority of the events are triggered by the movement of the quadrotor since it is the only object in the scene that changes brightness or motion. Therefore, the event reconstruction frames mainly consist of a gray background with an event blob triggered by the target. With good lighting conditions and a simple background, the target is easily distinguishable in both frames and event data (see Figure 5a). The advantage of our proposed filter over frame-based algorithms becomes more apparent in low-light conditions or environments with complex backgrounds. As shown in Figure 5b), the complex background in the



Figure 7: Example of the estimated trajectory by our filter and the 3D GPS trajectory in a 3D plot. The first row shows the estimated trajectory (marked by red dots) of the tracked quadrotor overlaid on the event reconstruction frames. The second row shows the 3D GPS data of the full trajectory. The camera position and East-North-Height direction are marked at the bottom.

frames makes tracking using RGB frames extremely challenging when the quadrotor crosses trees. In contrast, our filter can still track the quadrotor successfully because the spinning rotors and the motion of the quadrotor generates sufficient events for the filter to clearly distinguish it from the background. In the poorly lit sequences in Figure 5c)-d), the RGB frames only capture a faint green light emitted by an LED on the quadrotor, making tracking nearly impossible. On the other hand, the event camera can still capture unique event blobs of the quadrotor even in low light or in front of a complex background, providing sufficient information for our filter to achieve reliable tracking performance even in these challenging scenarios.

In the third column in Figure 5, when the camera is also moving, the background triggers many events, posing a challenge for tracking. The dynamic nearest neighbour data association approach (cf. Section 5.3) selectively feeds events to the filter based on their proximity to the centre of the target and estimation of the target size. Only events within a dynamic threshold from the target’s centre are considered, effectively rejecting the vast majority of background noise. Although overall the tracking performance is excellent, the present algorithm can still lose track if substantial ego-motion of the camera occurs just as the target crosses a high contrast feature in the scene. This is particularly the case if the camera ego-motion tracks the target, since this reduces the optical flow of the target and increases the optical flow of the scene. In such situations, a scene feature blob can capture the filter state and draw it away from the target. Interestingly, this scenario is almost always related to the rotational ego-motion of the camera, since such motion generates the majority of optical flow in a scene. The corresponding filter velocity of the incorrect blob track could then be computed *a-priori* from the angular velocity of the camera, and this prior information could be exploited to reject false background tracks. Implementation of this concept is beyond the scope of the present paper but is relevant in the context of the future potential of the algorithm.

### 6.3.1 Qualitative Tracking Performance

To provide a qualitative measure of tracking performance we have overlaid the estimated trajectory of the tracked quadrotor on event reconstructions (obtained using the event-based high-pass filter [46]) during aerobic manoeuvres. In Figure 7, red dots represent the continuous-time trajectory estimated by our filter while the background frames show the reconstructed intensity image from events. The close alignment between the red estimated trajectory and the observed event trajectory shows that our filter accurately tracks the trajectory of the target quadrotor. The quadrotor was also equipped with RTK-GPS and the full 3D trajectory is shown as an orange trajectory in the perspective image in Figure 7. The corresponding zigzag and “E” sub-trajectories are indicated in yellow. The camera position and East-North-Height direction are marked at the bottom right of the figure.

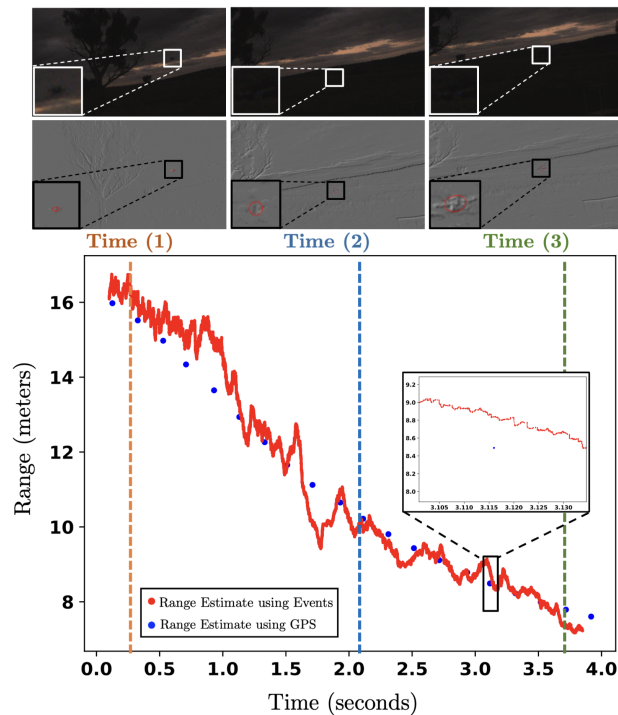


Figure 8: Range estimation of an approaching quadrotor in a low-light environment using events and GPS data. The first and second rows show the reference RGB images and event reconstructions. The estimated position and shape using events are represented by red ellipses on event reconstructions. The third row shows the continuous-time range estimate along with a zoom-in plot illustrating a short period. The estimated range aligns with the range estimation using GPS data and achieves more than a 50kHz update.

### 6.3.2 Range Estimation

The shape parameters estimated in the proposed filter allow us to derive an estimate of range for a known physical target. The target shape parameters  $(\lambda_k^1, \lambda_k^2)$  encode the visual second-order moment of the event blob. Since the quadrotor is disc shaped, the maximum of the visual second-order moment is visually related to the diameter of the quadrotor. By triangulation, the range can be estimated by

$$\text{Range} = \frac{af}{\max(\lambda_k^1, \lambda_k^2)}, \quad (28)$$

where  $a$  is the actual diameter of the target in meters and  $f$  is the camera focal length.

We provide an example of range estimation for a quadrotor as it approaches the camera location in low-light conditions from a distance of approximately 17 meters to a distance of less than 8 meters in Figure 8. The image data is shown at three time-stamps each indicated by a different colour while the detailed range estimation data is shown in red in the following graph. The reference data points (in blue) are computed from RTK-GPS log from the vehicle compared to a known GPS location of the camera. Note that the RTK-GPS is only available at 5Hz and our filter achieves more than a 50kHz update.

The quadrotor is almost impossible to visually identify or track using the dark RGB images in Figure 8. This is particularly the case when it flies in front of the dark mountains in the background. The precision of the proposed range information is strongly coupled with the high filter update rates that allow for temporal smoothing of the inferred shape parameters. In particular, even though the virtual measurement function based on the chi-squared statistic does involve temporal averaging, the time window on which this statistic is computed is so short (due to the high filter update rate) compared to the vehicle dynamics that the proposed range estimate is remarkably reliable.

## 7 Conclusion

This paper presents a novel filtering algorithm for tracking event blobs asynchronously in real time. The proposed filter achieves accurate tracking and blob shape estimation even under low-light environments and high-speed motion. It fully exploits the advantages of events by processing each event and updating the filter state asynchronously, achieving high temporal resolution state estimation (over 50kHz for the experiments undertaken). The high-rate, robust filter output directly enables downstream

tasks such as time-to-contact and range estimation, demonstrating the practical potential of the algorithm in a wide range of computer vision and robotics applications that require precise tracking and size estimation of fast-moving targets.

## 8 Acknowledgement

We sincerely thank Dr. Andrew Tridgell and Ms. Michelle Rossouw from the Ardupilot Community for their invaluable help collecting and processing the quadrotor dataset. Their expertise and dedication greatly contributed to this work.

## 9 Appendix

### 9.1 Proof of Lemma 4.1

The expressions for the pseudo measurements and their variances (i.e., the diagonal terms of  $R$ ) were established in Section 4.2. It remains only to show that the covariance (i.e., the off-diagonal terms of  $R$ ) of the measurements is zero.

The covariance of  $H_k$  and  $G_k$  is defined as [47]

$$\begin{aligned} \text{Cov}(H_k, G_k) &= E[(H_k - E[H_k])(G_k - E[G_k])] \\ &= E[H_k G_k - E[H_k]G_k - H_k E[G_k] + E[H_k]E[G_k]]. \end{aligned} \quad (29)$$

According to (11)-(17), the expected value  $E[H_k] = [0, 0]^\top$  and  $E[G_k] = 2n$ . It follows that

$$\begin{aligned} &E[H_k G_k - E[H_k]G_k - H_k E[G_k] + E[H_k]E[G_k]] \\ &= E[H_k G_k - 2nH_k] \\ &= E[H_k G_k] - 2nE[H_k] \\ &= E[H_k G_k]. \end{aligned}$$

By the law of total expectation, we have that

$$\begin{aligned} E[H_k G_k] &= E[E[H_k G_k | x_k]], \\ &= E\left[E\left[\begin{pmatrix} h_{p_x}(t_k) \\ h_{p_y}(t_k) \end{pmatrix} G_k \middle| x_k\right]\right]. \end{aligned} \quad (30)$$

Note that  $h_{p_x}(t_k)$  and  $h_{p_y}(t_k)$  are independent given  $x_k$  because they are jointly Gaussian with the covariance of  $H(x_k; \xi_k)$  being  $I_2$  by construction (see (11)). Thus, we may consider the (conditional) expectations  $E[h_{p_x}(t_k)G_k | x_k]$  and  $E[h_{p_y}(t_k)G_k | x_k]$  separately.

Expanding the first term  $E[h_{p_x}(t_k)G_k | x_k]$ , we have

$$\begin{aligned} &E[h_{p_x}(t_k) [h_{p_x}^2(t_k) + h_{p_y}^2(t_k) + \sum_{j=2}^n \|\chi_{k-j+1}\|^2] | x_k] \\ &= E[h_{p_x}^3(t_k) | x_k] + E[h_{p_x}(t_k)h_{p_y}^2(t_k) | x_k] \\ &\quad + E[h_{p_x}(t_k) | x_k] E[\sum_{j=2}^n \|\chi_{k-j+1}\|^2 | x_k] \end{aligned} \quad (31)$$

where the equality holds due to the linearity of the (conditional) expectation operator, and by noting that  $h_{p_x}(t_k)$  and  $\chi_{k-j+1}$  for  $j > 1$  are conditionally independent given  $x_k$  since  $\chi_{k-j+1}$  is a function only of the (past) events  $\{\xi_1, \xi_2, \dots, \xi_{k-j+1}\}$  and  $h_{p_x}(t_k)$  is a function of the (current) event  $\xi_k$ . From the definition of  $h_{p_x}(t_k)$ , we further have that

$$\begin{aligned} E[h_{p_x}(t_k) | x_k] &= E[\Lambda_k^{-1}(\xi_x(t_k) - p_x(t_k)) | x_k] \\ &= \Lambda_k^{-1} E[\xi_x(t_k) | x_k] - \Lambda_k^{-1} p_x(t_k) \\ &= \Lambda_k^{-1} p_x(t_k) - \Lambda_k^{-1} p_x(t_k) \\ &= 0, \end{aligned} \quad (32)$$

where  $E[\xi_x(t_k) | x_k] = p_x(t_k)$  via (3), and

$$E[h_{p_x}(t_k)h_{p_y}^2(t_k) | x_k] = 0 \quad (33)$$

since  $h_{p_x}(t_k)$  and  $h_{p_y}(t_k)$  are independent given  $x_k$ . Substituting (32) and (33) into (31), we obtain

$$E[h_{p_x}(t_k)H_k | x_k] = E[h_{p_x}^3(t_k) | x_k]. \quad (34)$$

A similar argument for the second conditional expectation in equation (30) gives that  $E[h_{p_y}(t_k)G_k|x_k] = [h_{p_y}^3(t_k)|x_k]$ . Thus

$$\begin{aligned} \text{Cov}(H_k, G_k) &= E[H_k G_k] \\ &= E\left[\begin{pmatrix} E[h_{p_x}^3(t_k)|x_k] \\ E[h_{p_y}^3(t_k)|x_k] \end{pmatrix}\right] \\ &= E\left[\begin{pmatrix} h_{p_x}^3(t_k) \\ h_{p_y}^3(t_k) \end{pmatrix}\right] \\ &= \begin{pmatrix} 0 \\ 0 \end{pmatrix}. \end{aligned} \quad (35)$$

We have therefore established that there is no cross-correlation between  $H_k$  and  $G_k$ .

## 9.2 Partial Derivatives of Observation Model

The partial derivatives of  $H(x_k; \xi_k)$  and  $G(x_k; \xi_k, \hat{P}_k^-, \Xi_k)$  w.r.t.  $p_k$ ,  $v_k$  and  $\lambda_k$  are

$$\begin{aligned} D_{p_k} H(x_k; \xi_k) &= -\Lambda_k^{-1}, \\ D_{v_k} H(x_k; \xi_k) &= 0, \\ D_{\lambda_k} H(x_k; \xi_k) &= -\mathcal{R}(\theta_k) \text{diag}[\mu^2 \mathcal{R}(-\theta_k)(\xi_k - p_k)], \\ D_{\theta_k} H(x_k; \xi_k) &= \mathcal{R}(\theta_k)[\Omega \mu - \mu \Omega] \mathcal{R}(-\theta_k)(\xi_k - p_k), \\ D_{q_k} H(x_k; \xi_k) &= 0, \\ D_{p_k} G(x_k; \xi_k, \hat{P}_k^-, \Xi_k) &= 2(\Lambda_k^{-1}(\xi_k - p_k))^\top D_{p_k} H(x_k; \xi_k), \\ D_{v_k} G(x_k; \xi_k, \hat{P}_k^-, \Xi_k) &= 0, \\ D_{\lambda_k} G(x_k; \xi_k, \hat{P}_k^-, \Xi_k) &= 2(\Lambda_k^{-1}(\xi_k - p_k))^\top D_{\lambda_k} H(x_k; \xi_k) \\ &\quad - \frac{2}{1 + \beta} \sum_{j=2}^n \zeta, \\ D_{\theta_k} G(x_k; \xi_k, \hat{P}_k^-, \Xi_k) &= 2(\Lambda_k^{-1}(\xi_k - p_k))^\top D_{\theta_k} H(x_k; \xi_k), \\ D_{q_k} G(x_k; \xi_k, \hat{P}_k^-, \Xi_k) &= 0, \end{aligned} \quad (36)$$

where

$$\begin{aligned} \mu &:= \text{diag}^{-1}[\lambda_k^1, \lambda_k^2], \\ \Omega &= (0, -1; 1, 0), \\ \zeta &:= \chi_{k-j+1}^\top \mathcal{R}(\hat{\theta}_{k-n+1}^-) \text{diag}[\mu^2 \mathcal{R}(-\hat{\theta}_{k-n+1}^-)(\xi_k - \hat{p}_{k-j+1}^-)]. \end{aligned} \quad (37)$$

## References

- [1] G. Gallego, T. Delbrück, G. Orchard, C. Bartolozzi, B. Taba, A. Censi, S. Leutenegger, A. J. Davison, J. Conradt, K. Daniilidis, and D. Scaramuzza, “Event-based vision: A survey,” *IEEE transactions on pattern analysis and machine intelligence*, vol. 44, no. 1, pp. 154–180, 2020.
- [2] J. N. P. Martel, J. Müller, J. Conradt, and Y. Sandamirskaya, “An active approach to solving the stereo matching problem using event-based sensors,” in *IEEE Int. Symp. Circuits Syst. (ISCAS)*, 2018, pp. 1–5.
- [3] Z. Wang, Y. Ng, P. van Goor, and R. Mahony, “Event camera calibration of per-pixel biased contrast threshold,” *Australasian Conference on Robotics and Automation, ACRA*, 2019.
- [4] T. Chin, S. Bagchi, A. P. Eriksson, and A. van Schaik, “Star tracking using an event camera,” in *IEEE Conf. Comput. Vis. Pattern Recog. Workshops (CVPRW)*, 2019.
- [5] T. Chin and S. Bagchi, “Event-based star tracking via multiresolution progressive hough transforms,” in *IEEE Winter Conf. Appl. Comput. Vis. (WACV)*, 2020.
- [6] Y. Ng, Y. Latif, T.-J. Chin, and R. Mahony, “Asynchronous kalman filter for event-based star tracking,” in *Computer Vision—ECCV 2022 Workshops: Tel Aviv, Israel, October 23–27, 2022, Proceedings, Part I*. Springer, 2023, pp. 66–79.
- [7] Z. Ni, C. Pacoret, R. Benosman, S.-H. Ieng, and S. Régnier, “Asynchronous event-based high speed vision for microparticle tracking,” *J. Microscopy*, vol. 245, no. 3, pp. 236–244, 2012.
- [8] D. Drazen, P. Lichtsteiner, P. Häfliger, T. Delbrück, and A. Jensen, “Toward real-time particle tracking using an event-based dynamic vision sensor,” *Experiments in Fluids*, vol. 51, no. 5, pp. 1465–1469, 2011.

- [9] Y. Wang, R. Idoughi, and W. Heidrich, “Stereo event-based particle tracking velocimetry for 3d fluid flow reconstruction,” in *Computer Vision—ECCV 2020: 16th European Conference, Glasgow, UK, August 23–28, 2020, Proceedings, Part XXIX 16*. Springer, 2020, pp. 36–53.
- [10] A. N. Angelopoulos, J. N. Martel, A. P. Kohli, J. Conradt, and G. Wetzstein, “Event based, near eye gaze tracking beyond 10,000 hz,” *arXiv preprint arXiv:2004.03577*, 2020.
- [11] C. Ryan, B. O’Sullivan, A. Elrasad, A. Cahill, J. Lemley, P. KIELTY, C. Posch, and E. Perot, “Real-time face & eye tracking and blink detection using event cameras,” *Neural Networks*, vol. 141, pp. 87–97, 2021.
- [12] A. Z. Zhu, N. Atanasov, and K. Daniilidis, “Event-based visual inertial odometry,” in *IEEE Conf. Comput. Vis. Pattern Recog. (CVPR)*, 2017, pp. 5816–5824.
- [13] —, “Event-based feature tracking with probabilistic data association,” in *IEEE Int. Conf. Robot. Autom. (ICRA)*, 2017, pp. 4465–4470.
- [14] J. Manderscheid, A. Sironi, N. Bourdis, D. Migliore, and V. Lepetit, “Speed invariant time surface for learning to detect corner points with event-based cameras,” in *IEEE Conf. Comput. Vis. Pattern Recog. (CVPR)*, 2019.
- [15] S. Hu, Y. Kim, H. Lim, A. J. Lee, and H. Myung, “ecdt: Event clustering for simultaneous feature detection and tracking,” in *2022 IEEE/RSJ International Conference on Intelligent Robots and Systems (IROS)*. IEEE, 2022, pp. 3808–3815.
- [16] N. Messikommer\*, C. Fang\*, M. Gehrig, and D. Scaramuzza, “Data-driven feature tracking for event cameras,” *IEEE Conference on Computer Vision and Pattern Recognition*, 2023.
- [17] X. Clady, S.-H. Ieng, and R. Benosman, “Asynchronous event-based corner detection and matching,” *Neural Netw.*, vol. 66, pp. 91–106, 2015.
- [18] I. Alzugaray and M. Chli, “Asynchronous corner detection and tracking for event cameras in real time,” *IEEE Robotics and Automation Letters*, vol. 3, no. 4, pp. 3177–3184, 2018.
- [19] F. Barranco, C. Fermuller, and E. Ros, “Real-time clustering and multi-target tracking using event-based sensors,” in *2018 IEEE/RSJ International Conference on Intelligent Robots and Systems (IROS)*. IEEE, 2018, pp. 5764–5769.
- [20] R. Li, D. Shi, Y. Zhang, K. Li, and R. Li, “Fa-harris: A fast and asynchronous corner detector for event cameras,” in *2019 IEEE/RSJ International Conference on Intelligent Robots and Systems (IROS)*. IEEE, 2019, pp. 6223–6229.
- [21] I. Alzugaray and M. Chli, “Haste: multi-hypothesis asynchronous speeded-up tracking of events,” in *31st British Machine Vision Virtual Conference (BMVC 2020)*. ETH Zurich, Institute of Robotics and Intelligent Systems, 2020, p. 744.
- [22] J. Duo and L. Zhao, “An asynchronous real-time corner extraction and tracking algorithm for event camera,” *Sensors*, vol. 21, no. 4, p. 1475, 2021.
- [23] D. Gehrig, H. Rebecq, G. Gallego, and D. Scaramuzza, “EKLT: Asynchronous photometric feature tracking using events and frames,” *Int. J. Comput. Vis.*, 2019.
- [24] E. Mueggler, N. Baumli, F. Fontana, and D. Scaramuzza, “Towards evasive maneuvers with quadrotors using dynamic vision sensors,” in *2015 European Conference on Mobile Robots (ECMR)*. IEEE, 2015, pp. 1–8.
- [25] A. Mitrokhin, C. Fermuller, C. Parameshwara, and Y. Aloimonos, “Event-based moving object detection and tracking,” in *IEEE/RSJ Int. Conf. Intell. Robot. Syst. (IROS)*, 2018.
- [26] D. Falanga, S. Kim, and D. Scaramuzza, “How fast is too fast? the role of perception latency in high-speed sense and avoid,” *IEEE Robotics and Automation Letters*, vol. 4, no. 2, pp. 1884–1891, 2019.
- [27] D. Falanga, K. Kleber, and D. Scaramuzza, “Dynamic obstacle avoidance for quadrotors with event cameras,” *Science Robotics*, vol. 5, no. 40, p. eaaz9712, 2020.
- [28] N. J. Sanket, C. M. Parameshwara, C. D. Singh, A. V. Kuruttukulam, C. Fermüller, D. Scaramuzza, and Y. Aloimonos, “Evdodgenet: Deep dynamic obstacle dodging with event cameras,” in *2020 IEEE International Conference on Robotics and Automation (ICRA)*. IEEE, 2020, pp. 10 651–10 657.
- [29] J. P. Rodríguez-Gómez, A. G. Eguíluz, J. Martínez-de Dios, and A. Ollero, “Asynchronous event-based clustering and tracking for intrusion monitoring in uas,” in *2020 IEEE International Conference on Robotics and Automation (ICRA)*. IEEE, 2020, pp. 8518–8524.
- [30] H. Li and L. Shi, “Robust event-based object tracking combining correlation filter and cnn representation,” *Frontiers in neurorobotics*, vol. 13, p. 82, 2019.
- [31] H. Chen, Q. Wu, Y. Liang, X. Gao, and H. Wang, “Asynchronous tracking-by-detection on adaptive time surfaces for event-based object tracking,” in *Proceedings of the 27th ACM International Conference on Multimedia*, 2019, pp. 473–481.
- [32] B. Ramesh, S. Zhang, Z. W. Lee, Z. Gao, G. Orchard, and C. Xiang, “Long-term object tracking with a moving event camera,” in *British Mach. Vis. Conf. (BMVC)*, 2018.
- [33] H. Chen, D. Suter, Q. Wu, and H. Wang, “End-to-end learning of object motion estimation from retinal events for event-based object tracking,” in *Proceedings of the AAAI Conference on Artificial Intelligence*, vol. 34, no. 07, 2020, pp. 10 534–10 541.



- [34] J. Zhang, B. Dong, H. Zhang, J. Ding, F. Heide, B. Yin, and X. Yang, “Spiking transformers for event-based single object tracking,” in *Proceedings of the IEEE/CVF conference on Computer Vision and Pattern Recognition*, 2022.
- [35] Z. Zhu, J. Hou, and X. Lyu, “Learning graph-embedded key-event back-tracing for object tracking in event clouds,” *Advances in Neural Information Processing Systems*, vol. 35, pp. 7462–7476, 2022.
- [36] J. Zhang, X. Yang, Y. Fu, X. Wei, B. Yin, and B. Dong, “Object tracking by jointly exploiting frame and event domain,” in *Proceedings of the IEEE/CVF International Conference on Computer Vision*, 2021, pp. 13 043–13 052.
- [37] C. Iaboni, D. Lobo, J.-W. Choi, and P. Abichandani, “Event-based motion capture system for online multi-quadrotor localization and tracking,” *Sensors*, vol. 22, no. 9, p. 3240, 2022.
- [38] G. R. Müller and J. Conradt, “A miniature low-power sensor system for real time 2d visual tracking of led markers,” in *2011 IEEE International Conference on Robotics and Biomimetics*. IEEE, 2011, pp. 2429–2434.
- [39] A. Censi, J. Strubel, C. Brandli, T. Delbruck, and D. Scaramuzza, “Low-latency localization by active LED markers tracking using a dynamic vision sensor,” in *IEEE/RSJ Int. Conf. Intell. Robot. Syst. (IROS)*, 2013.
- [40] Z. Wang, Y. Ng, J. Henderson, and R. Mahony, “Smart visual beacons with asynchronous optical communications using event cameras,” in *International Conference on Intelligent Robots and Systems (IROS 2022)*, 2022.
- [41] Z. Wang, D. Yuan, Y. Ng, and R. Mahony, “A linear comb filter for event flicker removal,” in *International Conference on Robotics and Automation (ICRA)*, 2022.
- [42] M. Delbraccio, P. Musé, A. Almansa, and J.-M. Morel, “The non-parametric sub-pixel local point spread function estimation is a well posed problem,” *International journal of computer vision*, pp. 1–20, 2011.
- [43] Z. Wang, Y. Ng, C. Scheerlinck, and R. Mahony, “An asynchronous kalman filter for hybrid event cameras,” in *Int. Conf. Comput. Vis. (ICCV)*, 2021.
- [44] S. J. Julier and J. J. LaViola, “On kalman filtering with nonlinear equality constraints,” *IEEE transactions on signal processing*, vol. 55, no. 6, pp. 2774–2784, 2007.
- [45] G. E. Box, W. H. Hunter, S. Hunter, *et al.*, *Statistics for experimenters*. John Wiley and sons New York, 1978, vol. 664.
- [46] C. Scheerlinck, N. Barnes, and R. Mahony, “Continuous-time intensity estimation using event cameras,” in *Asian Conference on Computer Vision*. Springer, 2018, pp. 308–324.
- [47] M. J. Schervish and M. H. DeGroot, *Probability and statistics (4th ed.)*. Pearson Education, 2012.